

Supporting Information

One-step construction of silver-polyaniline nanocomposite modified multifunctional sponges for wastewater remediation: adsorption, catalysis and antimicrobial applications

Huilin Song,^a Kaidi Zhang,^a Peiqi Li,^a Guowen Qin,^a Wanxin Xiao,^a Changdong Zhang,^a Yang Zheng,^b Yang Ding,^{*c} Shunli Ji^{*a}

^a*Department of Pharmaceutical Analysis, China Pharmaceutical University, No.24, Tongjiaxiang, Nanjing 210009, China*

^b*CR Medicon (Nanjing) Biotechnology Co., Ltd, No.18, Zhilan Road, Nanjing, 210009, China*

^c*Key Laboratory of Drug Quality Control and Pharmacovigilance (Ministry of Education), State Key Laboratory of Natural Medicines, Department of Pharmaceutics, NMPA Key Laboratory for Research and Evaluation of Pharmaceutical Preparations and Excipients, China Pharmaceutical University, Nanjing 210009, China*

*Corresponding authors

E-mail address: dingypharm@cpu.edu.cn (Y. Ding); 1020162527@cpu.edu.cn (S. Ji).

Text S1: Chemicals and Apparatus

1.1 Chemicals

Aniline, ammonium persulfate (APS), potassium persulfate (PDS), tertiary butyl alcohol (TBA), sodium sulfate (Na_2SO_4), silver nitrate (AgNO_3), lemon yellow (LY), amaranth and methylene blue (MB) were obtained from Aladdin (Shanghai, China). Hydrochloric acid (HCl), nitric acid (HNO_3), sulfuric acid (H_2SO_4), sodium chloride (NaCl), calcium chloride (CaCl_2) and P-benzoquinone (PBA) were purchased from Sinopharm Chemical Reagent (Shanghai, China). New carmine red (NC), allura red and sunset yellow were purchased from Shanghai Yuanye Biotechnology (Shanghai, China). The methyl violet (MV) was procured from Tianjin Chemical Reagent Research Institute (Tianjin, China) and erythrosine B sodium salt was obtained from Macklin (Shanghai, China). Ethanol (EtOH) and L-histidine (His) were purchased from Shanghai Lingfeng Chemical Reagent and Huixing Biochemical Reagent, respectively (Shanghai, China). The melamine sponges (MS), polyvinyl alcohol sponges (PAS) and polyurethane sponges (PUS) were obtained from Alibaba. The ultrapure water was from a Millipore Direct-Q3 purification system.

1.2 Apparatuses

Scanning electron microscopy (SEM) images taken with a JSM-6700F microscope were used to detect the surface morphology of sponge samples. Elemental analysis was performed using an Oxford X-ManN energy-dispersive X-ray spectroscopy (EDX). Element mapping images and energy spectra of the selected areas were conserved. The FTIR spectra were obtained from a Bruker Alpha II spectrometer by applying the Attenuated Total Reflection (ATR) mode in the range of $4000\text{--}400\text{ cm}^{-1}$ and X-ray photoelectron spectrometer (XPS) was achieved by a ThermoFischer ESCALAB 250XI with an Al $K\alpha$ radiation ($h\nu=1486.6\text{ eV}$) to recognize the different chemical composition of the sponges. The RIGAKU X-ray diffraction (XRD) smart X-ray polycrystalline diffractometer SmartLab was used to determine the crystallinity of sponges with Cu $K\alpha$ radiation ($\lambda = 1.54\text{ \AA}$) in 2θ ranges from 10° to 80° . The zeta potential was measured by Zetasizer Nano ZS90. The mechanical properties of samples were tested

using a ZQ-990A-1 rigid foam compression performance test machine. The compressive mechanical tests were implemented by compressing sponges along vertical axis with a constant deformation speed of 10 mm·min⁻¹. The response of sponges to different strains (20%, 50% and 70%) was examined and loading-unloading cycles were performed 50 times to check out the mechanical stability of the sponge at a constant strain of 70%. The electron paramagnetic resonance (EPR) experiments were performed on the Bruker spectrometer with 2,2,6,6-tetramethylpiperidine (TEMP) and 5,5-dimethyl-1-pyrroline N-oxide (DMPO) as the spin-trapping agents. Electrochemical tests were performed with a CHI 660C electrochemical analyzer. The specific intermediates of NC were analyzed by a LC-MS/MS system of Thermo Scientific, which was performed in the negative ion mode with an electrospray ionization (ESI) source. The photothermal effect was induced by a Ningbo Yuanming LSR808H-10W-FC fiber-coupled diode laser system. And the change in temperature was recorded every 3 s with a Fotric 226S thermal imaging camera.

Text S2: Adsorption isotherms and kinetic models

1. Adsorption isotherms

The linear forms of adsorption isotherm models were used to investigate the specific relationship between the adsorbate and adsorbent. Langmuir isotherm model assumes the adsorbent has homogeneous surface with identical adsorption sites and only can be covered by a complete monolayer, which can be expressed by:

$$\frac{C_e}{Q_e} = \frac{1}{K_L Q_m} + \frac{C_e}{Q_m} \quad (1)$$

Where C_e (mg·L⁻¹) is the total concentration of NC at equilibrium, Q_e (mg·g⁻¹) is the total adsorption capacity of NC at equilibrium, Q_m (mg·g⁻¹) is the maximum calculated adsorption capacity of sorbent, K_L (L·mg⁻¹) is the Langmuir constant. Besides, the separation factor of Langmuir model, R_L , which can reflex the essential characteristics of the

Langmuir isotherm, can be expressed as followed:

$$R_L = \frac{1}{1 + K_L C} \quad (2)$$

Where C is the initial concentration of NC (mg L^{-1}) and the value of R_L can indicate the type of isotherm: irreversible ($R_L = 0$), favorable ($0 < R_L < 1$), linear ($R_L = 1$), or unfavorable ($R_L > 1$).

Furthermore, the empirical Freundlich isotherm assumes the adsorbent has heterogeneous adsorbent surface with non-uniform adsorption sites, and describes reversible adsorption process. The Freundlich isotherm can be expressed by:

$$\ln Q_e = \ln K_F + \frac{\ln C_e}{n} \quad (3)$$

Where K_F and n are Freundlich constants parameters that related to sorption capacity and sorption intensity, when $0.1 < 1/n < 0.5$, it is easy to adsorb; when $0.5 < 1/n < 1$, there is a difficulty with the adsorption; when $1/n > 1$, it is quite difficult to adsorb.

2. Kinetic studies

New carmine solution with $40 \mu\text{mol}\cdot\text{L}^{-1}$ concentration was absorbed by Ag-PANI@PAS sponges and sampling at 5 s, 10 s, 20 s, 30 s, 1 min, 2 min, 5 min, 10 min, 20 min, 30 min, 60 min, 120 min. The UV absorbance of the supernatant was measured at 505 nm. The pseudo-first-order rate equation used for the adsorption of a solute from a liquid solution and can be expressed by:

$$\ln(Q_e - Q_t) = \ln Q_e - k_1 t \quad (4)$$

While the pseudo-second-order rate equation is based on adsorption equilibrium capacity and can be expressed by:

$$\frac{t}{Q_t} = \frac{1}{k_2 Q_e^2} + \frac{t}{Q_e} \quad (5)$$

Where Q_e ($\text{mg}\cdot\text{g}^{-1}$) is equilibrium absorption capacity; Q_t ($\text{mg}\cdot\text{g}^{-1}$) is adsorption amount at t min; k_1 (min^{-1}) is pseudo-first-order rate constant, and k_2 ($\text{g}\cdot\text{mg}^{-1}\cdot\text{min}^{-1}$) is pseudo-second-order rate constant.

The Weber-Morris intraparticle diffusion model can be expressed as:

$$Q_t = k_{dif}t^{1/2} + C \quad (6)$$

Where K_{dif} ($\text{mg g}^{-1} \text{min}^{-1/2}$) is the intraparticle diffusion rate constant, C (mg g^{-1}) is the intercept, which reflects the thickness of the boundary layer and the contribution of the surface sorption in the rate-limiting step.

Text S3: Catalytic kinetics

The primary kinetic model for catalytic process can be expressed by:

$$-\ln \frac{C_t}{C_0} = k_1 t \quad (7)$$

Where C_0 ($\text{mg}\cdot\text{L}^{-1}$) is the initial concentration of NC, C_t ($\text{mg}\cdot\text{L}^{-1}$) is the concentration of dye at time t (min) and k_1 is the degradation rate constant (min^{-1}).

While the secondary kinetic model for catalytic process can be expressed by:

$$\frac{1}{C_t} - \frac{1}{C_0} = k_2 t \quad (8)$$

Where C_0 ($\text{mg}\cdot\text{L}^{-1}$) is the initial concentration of NC, C_t ($\text{mg}\cdot\text{L}^{-1}$) is the concentration of dye at time t (min) and k_2 is the degradation rate constant ($\text{L}\cdot\text{mg}^{-1}\cdot\text{min}^{-1}$).

Text S4: UV-Vis spectra changes after Ag-PANI@PAS/PDS process

It is known that many metabolites of azo dyes can lead to potential health risks. Meanwhile, there were also situations where the color of the dye disappeared completely during the degradation process, but the toxic or genotoxic metabolites, unopened aromatic amines, were still remained¹. Therefore, the degraded metabolites were firstly monitored by UV-Vis spectroscopy. From Fig. S15, the characteristic peaks at 230, 320 and 510 nm were attributed to the vibration of phenyl, naphthyl, and azo bonds, respectively². During the degradation process, a complete decolorization of the NC solution could be observed in 12 min, as the dominant peak at 510 nm gradually

decreased. It could be seen that the absorbance at 230 nm increased slightly at 30 s, which indicated the formation of benzene intermediates. Meanwhile, the absorption peaks at 230 nm and 310 nm decreased slowly with time, suggesting the gradual cleavage of the aromatic rings. All intermediates were eventually mineralized to inorganic ions such as CO_2 and H_2O^3 . These findings implied the ecotoxicological safety of the degradation process by Ag-PANI@PAS.

Text S5: Possible degradation pathways in degradation system

In brief, the N=N (N(11) and N(12)) on NC was oxidized to form P1 and P2. As the bond length of C-S was usually long, the generation of P2 was accompanied by the disruption of both C(21)-S(24) and C(19)-S(25) bonds, and P1 was also further broken to produce P3. P2 can be transformed to P3 along with the removal of hydroxyl groups. Then, P3 could be oxidized to form P4 and P5 due to the high f_0 value of C(1,2,8,9). The high f_0 value of C(19,20) enabled P2 to undergo direct oxidation, leading to the formation of P6 and P7 through ring opening. Next, the above NC intermediates were further oxidized to small molecular organic compounds such as P8, P9 and P10. All intermediates were eventually mineralized to inorganic ions such as CO_2 and H_2O .

Text S6: Key parameters on catalytic performance

As shown in Fig. 8d, the degradation of NC was accelerated when PDS concentration increased from $0.625 \text{ g}\cdot\text{L}^{-1}$ to $5 \text{ g}\cdot\text{L}^{-1}$, with the removal efficiency of NC increasing from 72.4% to 95.7%. This discovery implies that the decolorization depended on the PDS concentration, as it could promote the adsorption of $\text{S}_2\text{O}_8^{2-}$ onto the active sites of Ag-PANI@PAS, resulting in the generation of more ROS (as described in Eq. (3-6)) and acceleration of the electron acceptance process, thus improving the degradation efficiency of NC. Taking economy into account, $2.5 \text{ g}\cdot\text{L}^{-1}$ PDS was chosen for subsequent experiments.

The solution pH is additionally a crucial factor in the degradation reaction, as pH will affect the conversion

between free radicals. Fig. 8e shows that the decolorization of NC was slightly inhibited under non-neutral conditions. Under acidic conditions, more $SO_4^{\cdot-}$ with high redox potential (2.6-3.1 V) could be produced to accelerate the degradation of NC, as described in Eq. (9-10). However, the lower adsorption of NC on Ag-PANI@PAS inhibited the degradation due to proton competition, especially for strongly acidic conditions. This further shows that adsorption is one of the key steps in achieving efficient catalytic degradation. Under alkaline conditions (pH > 7), the reaction between $SO_4^{\cdot-}$ and hydroxide ions generated $\cdot OH$, which actively participates in degradation processes, as described in Eq. (11). However, the redox potential of $\cdot OH$ (1.9-2.7 V) was lower than that of $SO_4^{\cdot-}$ (2.6-3.1 V), and the half-life of $\cdot OH$ (< 1 s) was also shorter compared to that of $SO_4^{\cdot-}$ (30-40 s). Consequently, the degradation efficiency of NC was slightly decreased when the pH > 7. Overall, the Ag-PANI@PAS/PDS system exhibited broad pH adaptability, highlighting its potential in a variety of practical wastewater treatments.



Text S7: Regeneration of Ag-PANI@PAS

The regeneration of Ag-PANI@PAS was firstly realized by traditional method. Firstly, Ag-PANI@PAS was adsorbed and saturated in 2 mL $80 \mu\text{mol}\cdot\text{L}^{-1}$ NC solution. Then, desorption was carried out twice for 3 min each with $1 \text{ mol}\cdot\text{L}^{-1}$ NaOH as desorbent, followed by activation with $1 \text{ mol}\cdot\text{L}^{-1}$ HCl, washed with ultrapure water and used for the next adsorption. Three adsorption/desorption cycles were performed.

As for the regeneration based on PDS activation, each adsorption experiment was carried out in 2 mL $200 \mu\text{mol}\cdot\text{L}^{-1}$ NC solution. Ag-PANI@PAS was firstly added to the above solution for saturated adsorption, which was then put into potassium persulfate solution for regeneration. The regenerated sponges was washed with ultrapure water

successively for dye adsorption again. Meanwhile, the effects of regeneration time (1-30 min), PDS concentration ($1 \text{ g}\cdot\text{L}^{-1}$ - $15 \text{ g}\cdot\text{L}^{-1}$) and cycle times were investigated. The regeneration efficiency (RE, %) was calculated as the evaluation index by the following Eq.:

$$RE(\%) = \frac{R_a}{R_b} \times 100\% \quad (12)$$

Where R_b and R_a are the removal efficiencies of the first adsorption and adsorption after regeneration.

Text S8: Relationship between adsorption and degradation

In view of the above experimental results, the intrinsic relationship between adsorption and degradation can be summarized as follows. The process of adsorption facilitates the rapid occurrence of catalytic degradation. Catalytic degradation in turn enables the treatment of high concentrations of dye wastewater (as shown in Fig. 7a and Video S4), and exhibits a broader range of substrate applicability, which effectively addresses the limitations associated with the adsorption method. In addition, green regeneration of adsorbents can be achieved by catalytic degradation. Compared with direct degradation in the solution system, degradation after adsorption can reduce the usage of PDS, lower the economic cost of wastewater treatment, and prevent the secondary pollution. The coordinated adsorption and catalytic functions of Ag-PANI@PAS make it promising for real application in wastewater treatment.

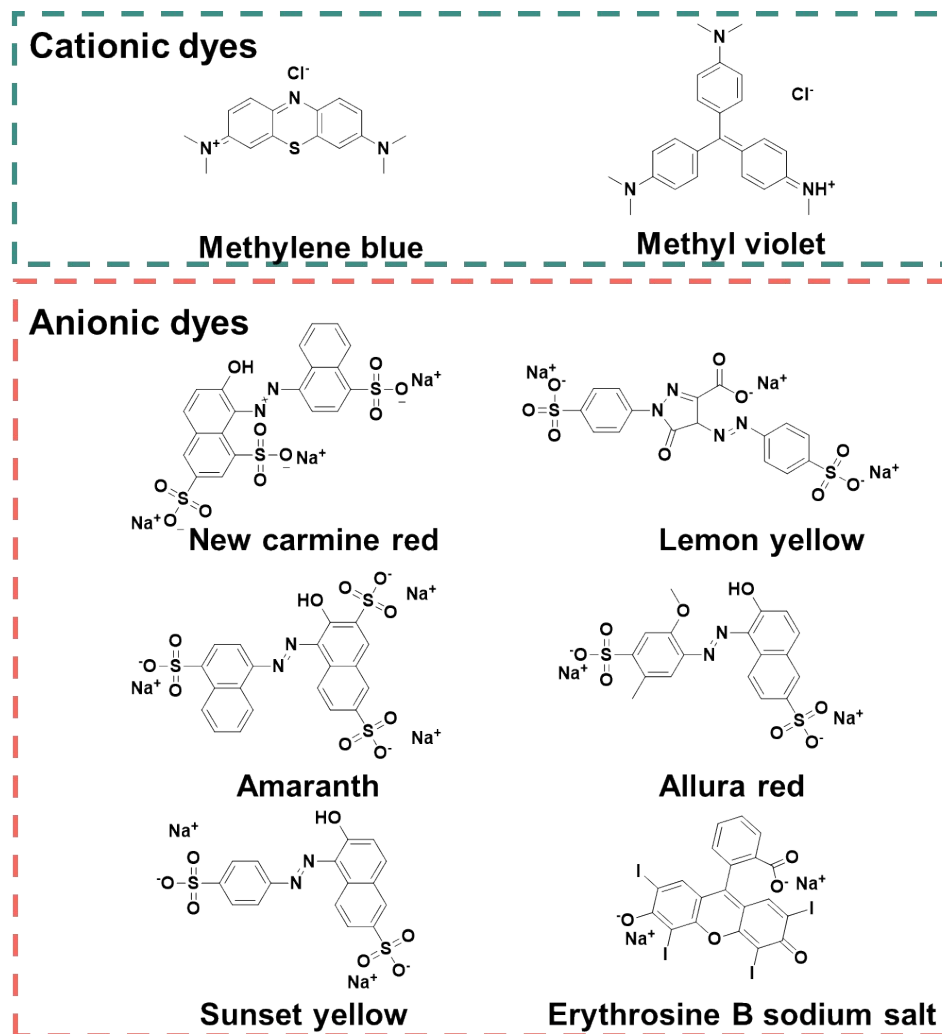


Fig. S1 The chemical structures of anionic and cationic dyes.

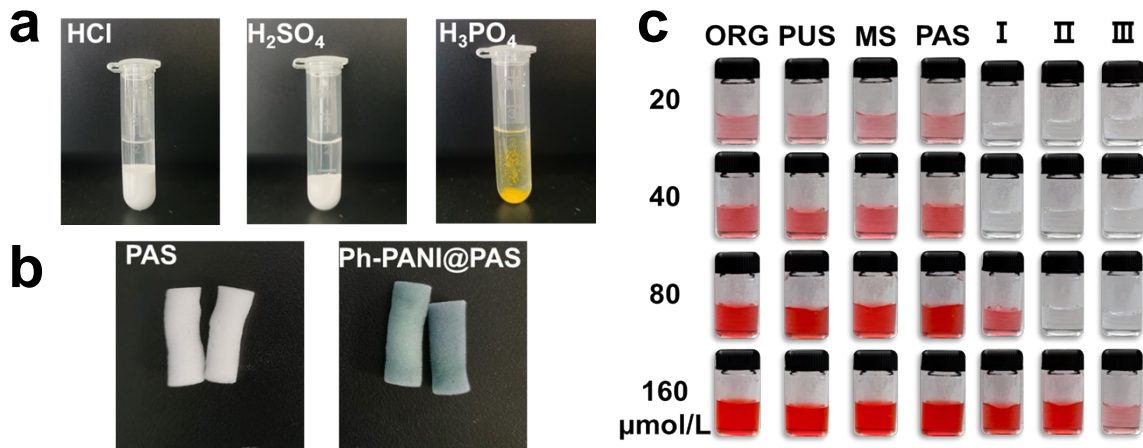


Fig. S2 (a) The digital photos of AgNO₃ in HCl, H₂SO₄ and H₃PO₄. (b) The photos of raw PAS and PANI@PAS prepared in phytic acid. (c) The photos of raw sponges and corresponding composite sponges (I: Ag-PANI@PUS, II: Ag-PANI@MS, III: Ag-PANI@PAS) for clean-up of NC dye solution at different concentrations.

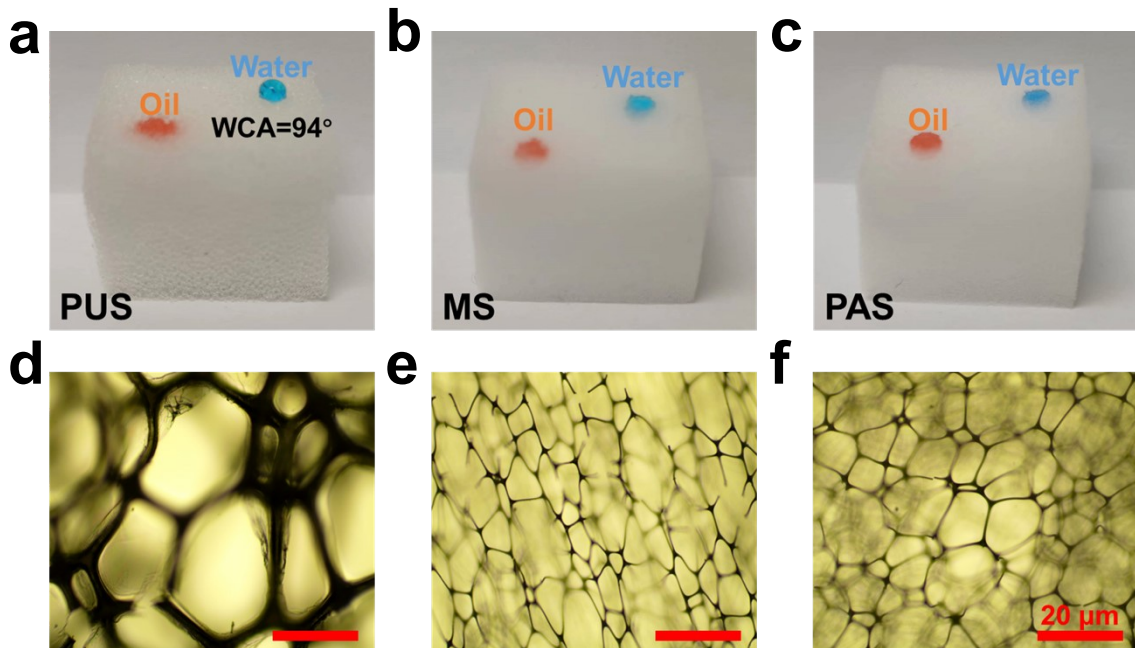


Fig. S3 The digital photos of water (dyed with methyl blue) and cyclohexane droplets (dyed with Sudan red III) on (a) PUS, (b) MS and (c) PAS. (d-f) The microscope images of raw PUS, MS and PAS.

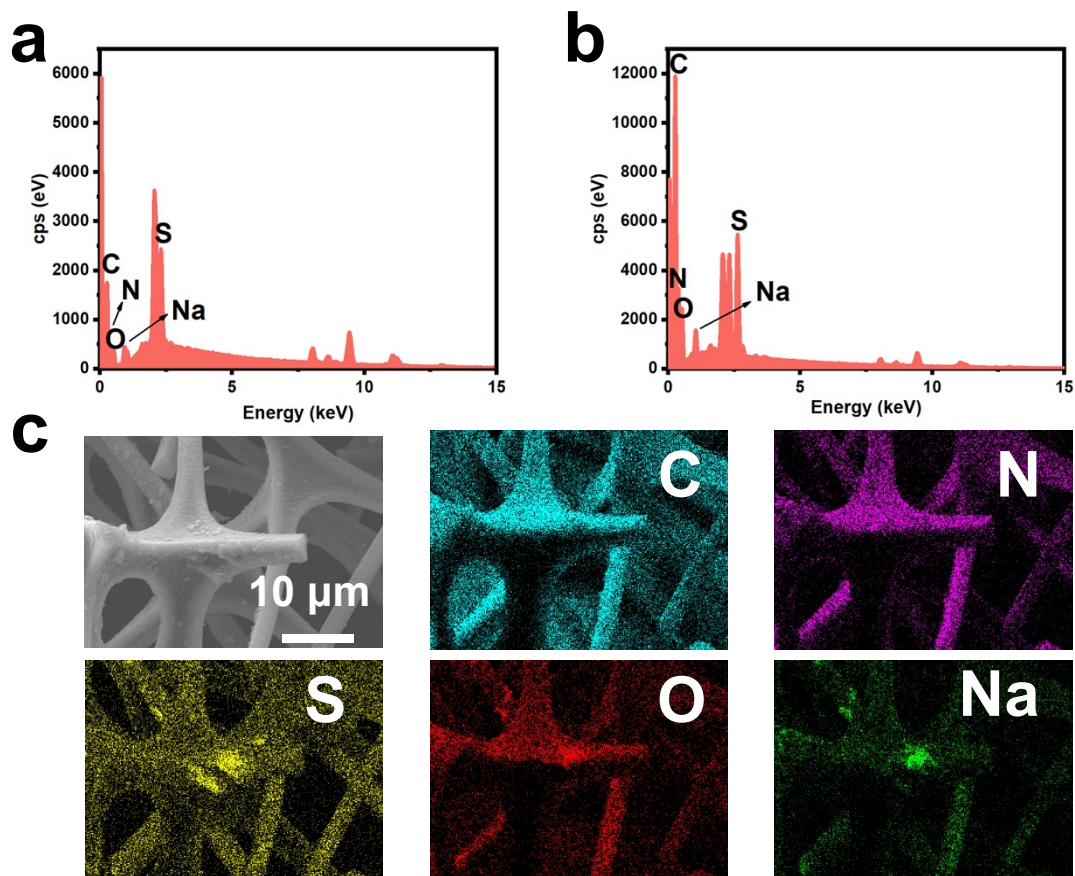


Fig. S4 (a and b) The EDX of PAS and PANI@PAS. (c) The EDX mapping of PANI@PAS.

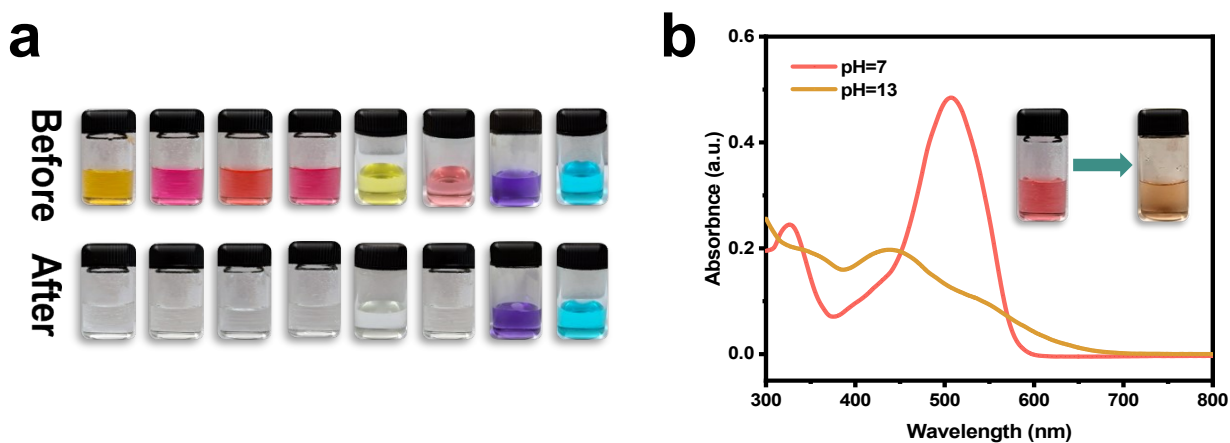


Fig. S5 (a) Digital photos of dye solutions before and after adsorption (Left to right: sunset yellow to methylene blue, in the same order as shown in Fig. 4c). (b) UV-vis spectra of NC solution at pH =7 and 13. The inset showed the digital photos.

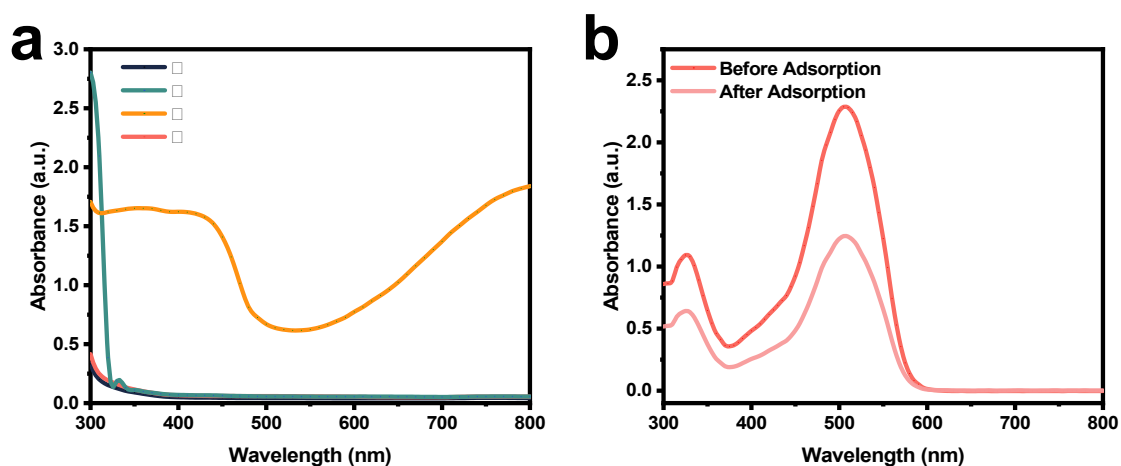


Fig. S6 (a) The UV-vis spectra of different material solutions (I: H₂O, II: aniline solution, III: Ag-PANI suspension, IV: the leaching solution of Ag-PANI@PAS). (b) The UV-vis spectra of NC solution (400 μmol·L⁻¹) before and after being adsorbed by Ag-PANI@PAS for 6 h.

Note: Good stability of the adsorbents in the adsorption medium is the key factor of its practical application. As displayed in Fig. S6a, no corresponding characteristic absorption appeared in the UV-vis spectrum of the 24 h leachate of Ag-PANI@PAS compared to those of the aniline solution and Ag-PANI suspension, which preliminarily proved the stability of Ag-PANI@PAS in the aqueous system. To confirm the stability during adsorption, the UV-vis spectra of NC solution before and after being adsorbed by Ag-PANI@PAS was measured (Fig. S6b). Compared with the initial solution, the peak of NC at 510 nm decreased after 6 h adsorption and no other peaks appeared in the spectra, which demonstrated that Ag-PANI coating did not dissolve in the solution when adsorption was performed. The above results prove the stability of Ag-PANI@PAS in dye solution and its applicability for water remediation.

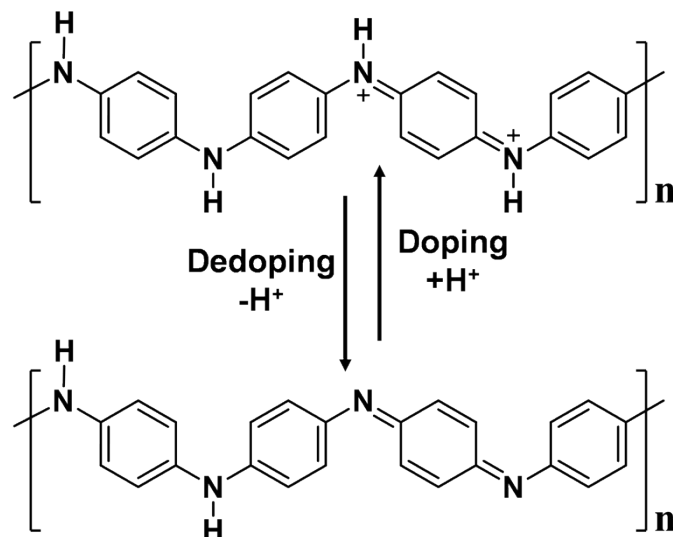


Fig. S7 The doping and dedoping processes of PANI.

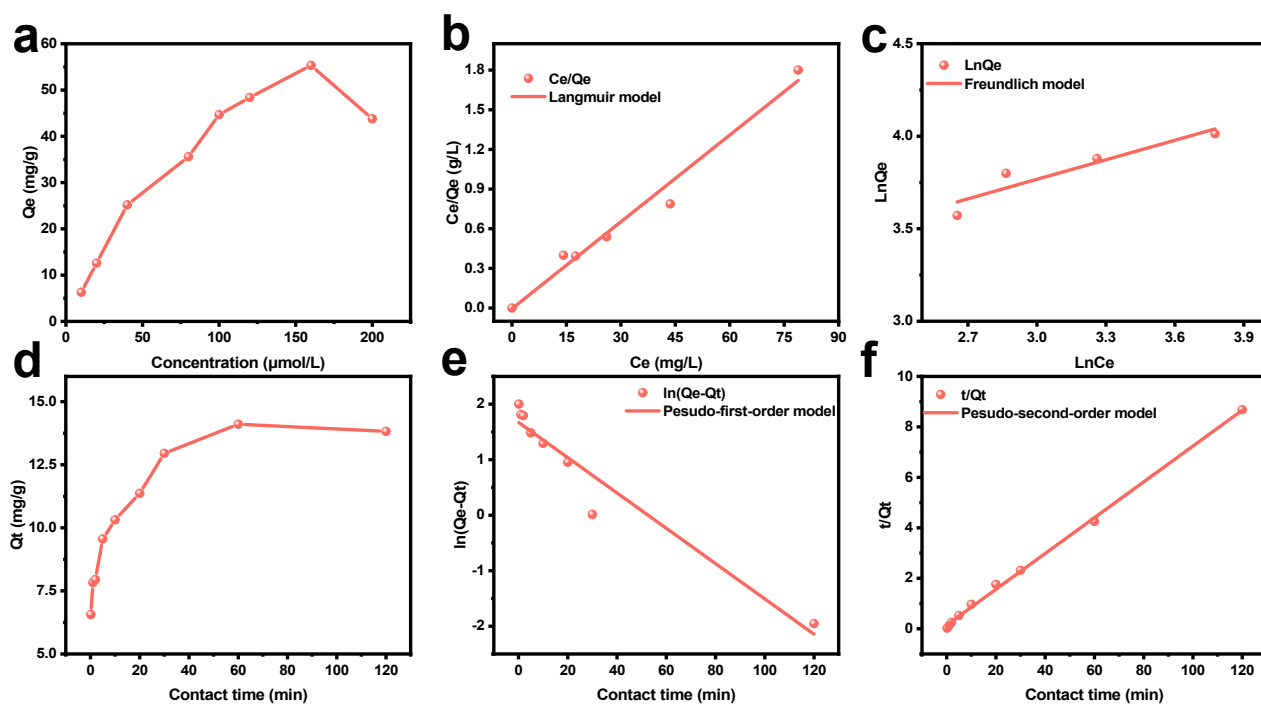


Fig. S8 (a) Effect of initial dye concentration on adsorption capacity of Ag-PANI@PAS. (b and c) Fitting curves of Langmuir and Freundlich isotherm models. (d) Effect of contact time on adsorption process. (e and f) Fitting curves of pseudo-first-order and pseudo-second-order kinetic models.

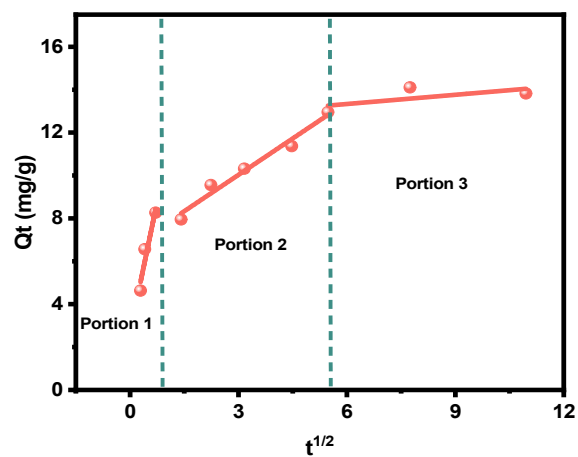


Fig. S9 Intraparticle diffusion plot of NC on Ag-PANI@PAS.

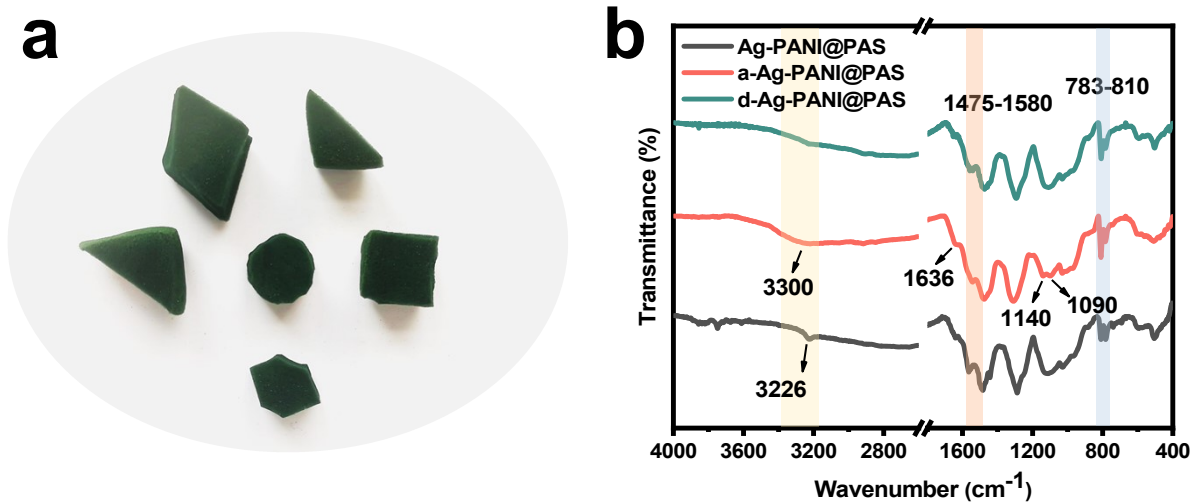


Fig. S10 (a) Different shapes of Ag-PANI@PAS. (b) FTIR spectra of Ag-PANI@PAS before, after adsorption (a-Ag-PANI@PAS) and after degradation (d-Ag-PANI@PAS).

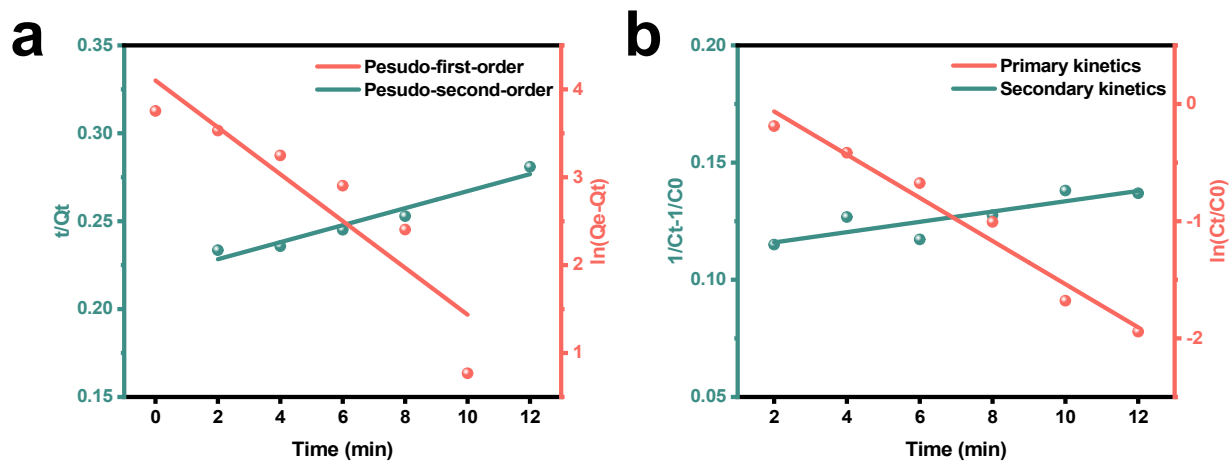


Fig. S11 (a and b) Fitting curves of adsorption kinetic models and catalytic kinetic models.

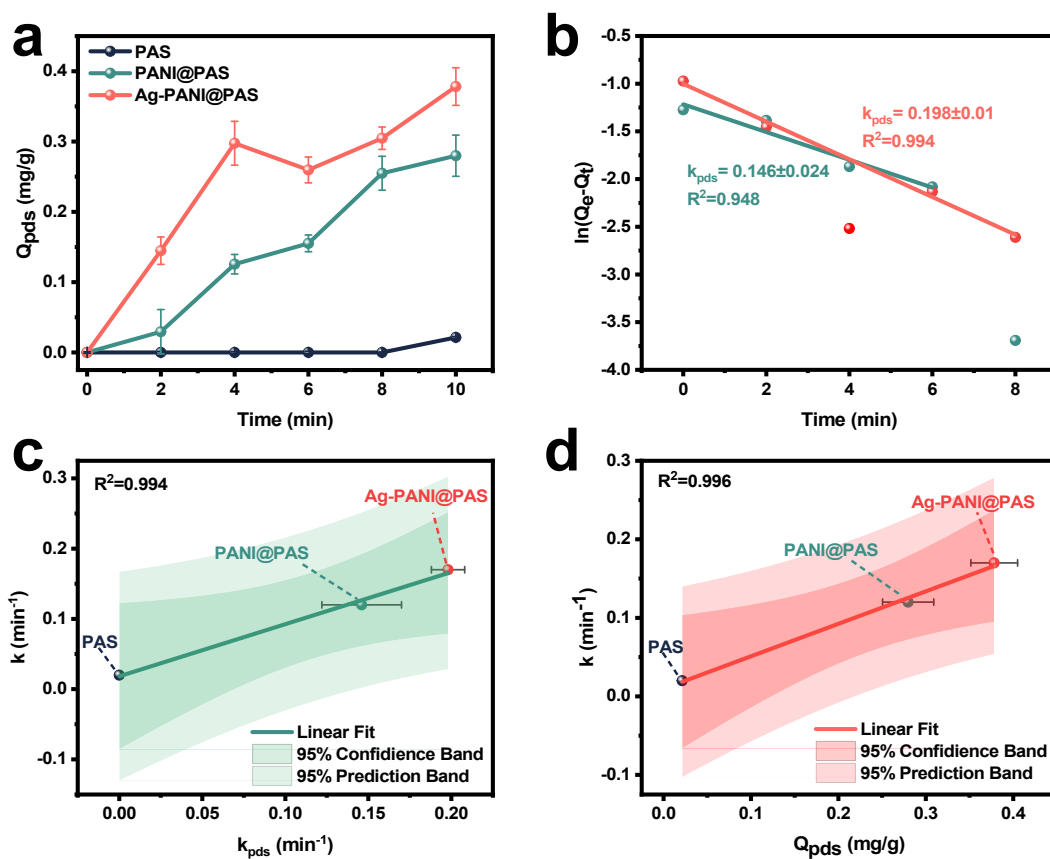
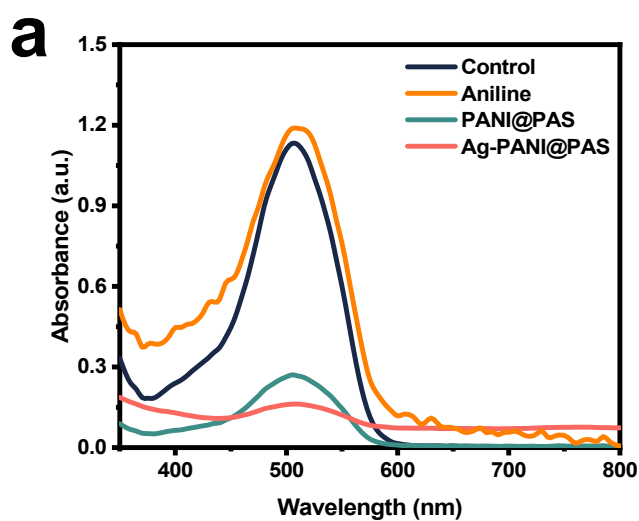


Fig. S12 (a) The adsorption of PDS by different sponges. (PDS loading: $2.5 \text{ g}\cdot\text{L}^{-1}$). (b) Fitting curves of pseudo-first-order kinetic model. (c) The correlation between the rate constants of PDS (k_{PDS}) and k (NC) for each system. (d) The correlation between the Q_{PDS} and k (NC).



b

	Removal efficiency (%)
Aniline	0
PANI@PAS	78.9
Ag-PANI@PAS	85.7

Fig. S13 (a) Compared catalytic performance for different catalysts (NC concentration: $200 \mu\text{mol}\cdot\text{L}^{-1}$, PDS loading: $2.5 \text{ g}\cdot\text{L}^{-1}$, aniline concentration: $0.16 \text{ mol}\cdot\text{L}^{-1}$). (b) The table showed the corresponding removal efficiency.

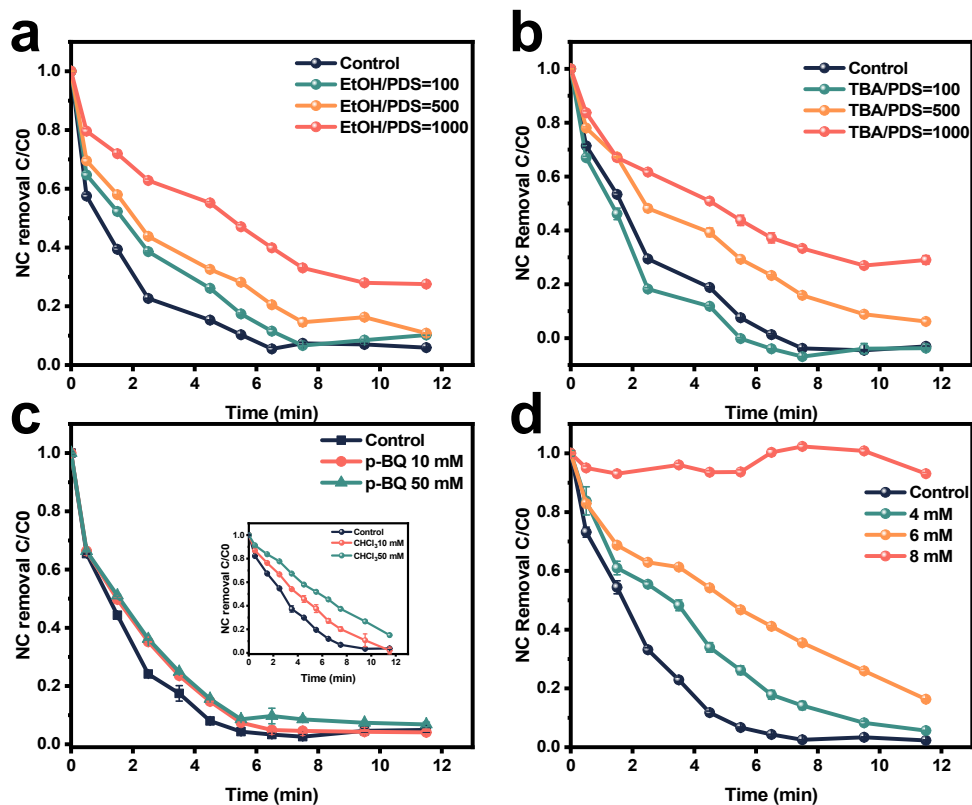


Fig. S14 Effect of EtOH (a), TBA (b), PBQ and CHCl_3 (c), and L-histidine (d) on NC degradation (NC concentration: $200 \mu\text{mol}\cdot\text{L}^{-1}$, PDS loading: $2.5 \text{ g}\cdot\text{L}^{-1}$).

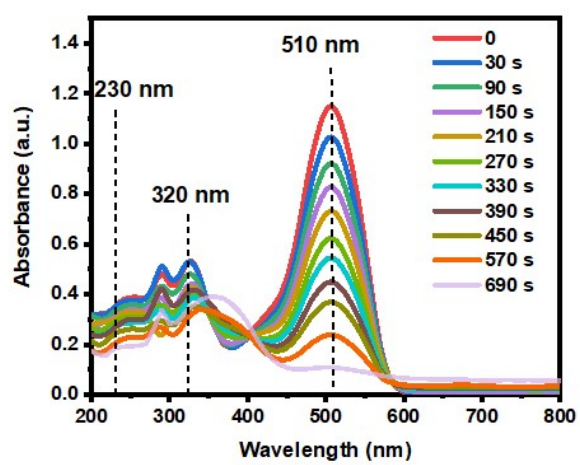


Fig. S15 UV-vis spectra changes during the process of Ag-PANI@PAS/PDS.

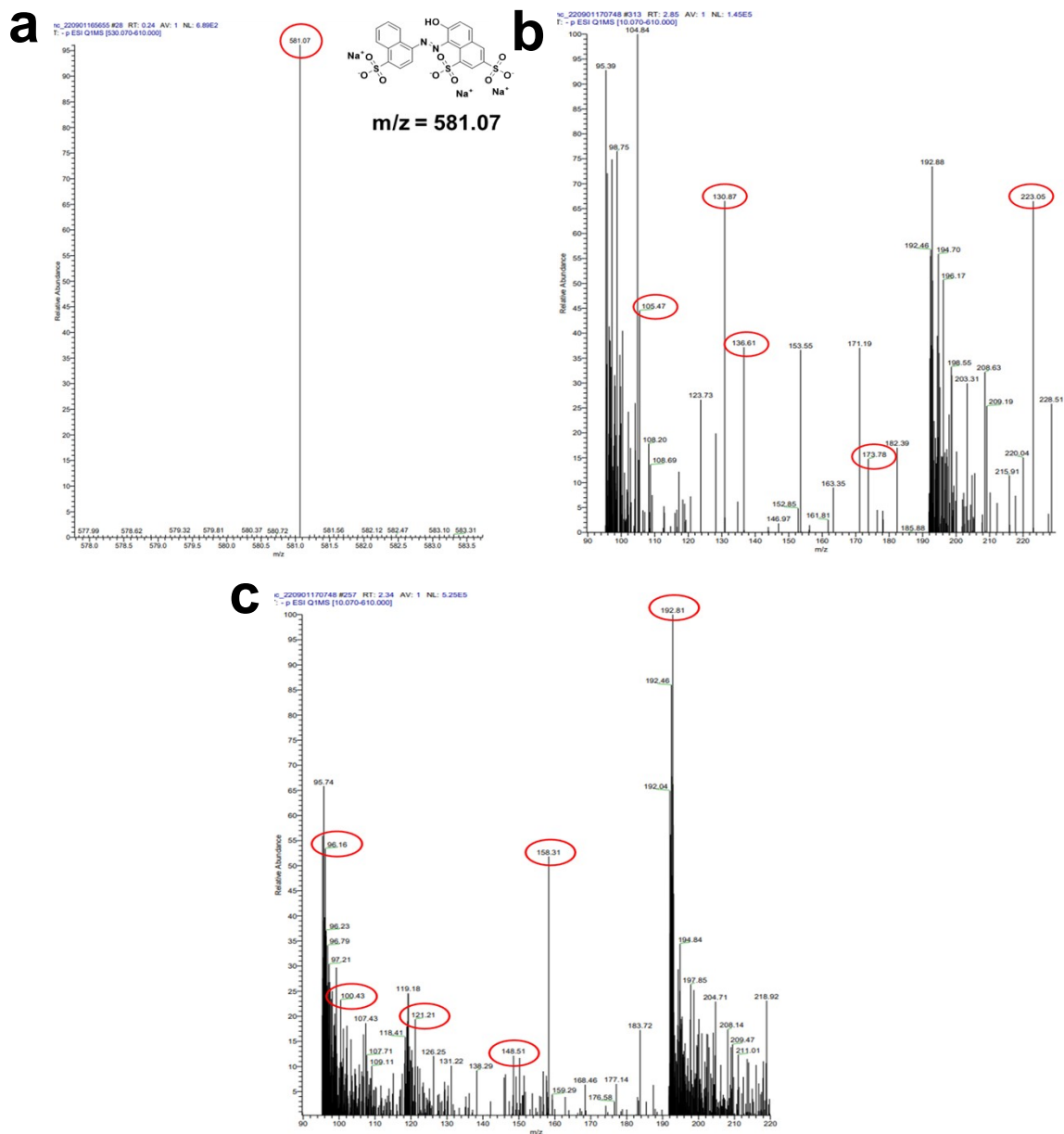


Fig. S16 MS spectra of NC (a) and its degradation products (b-c).

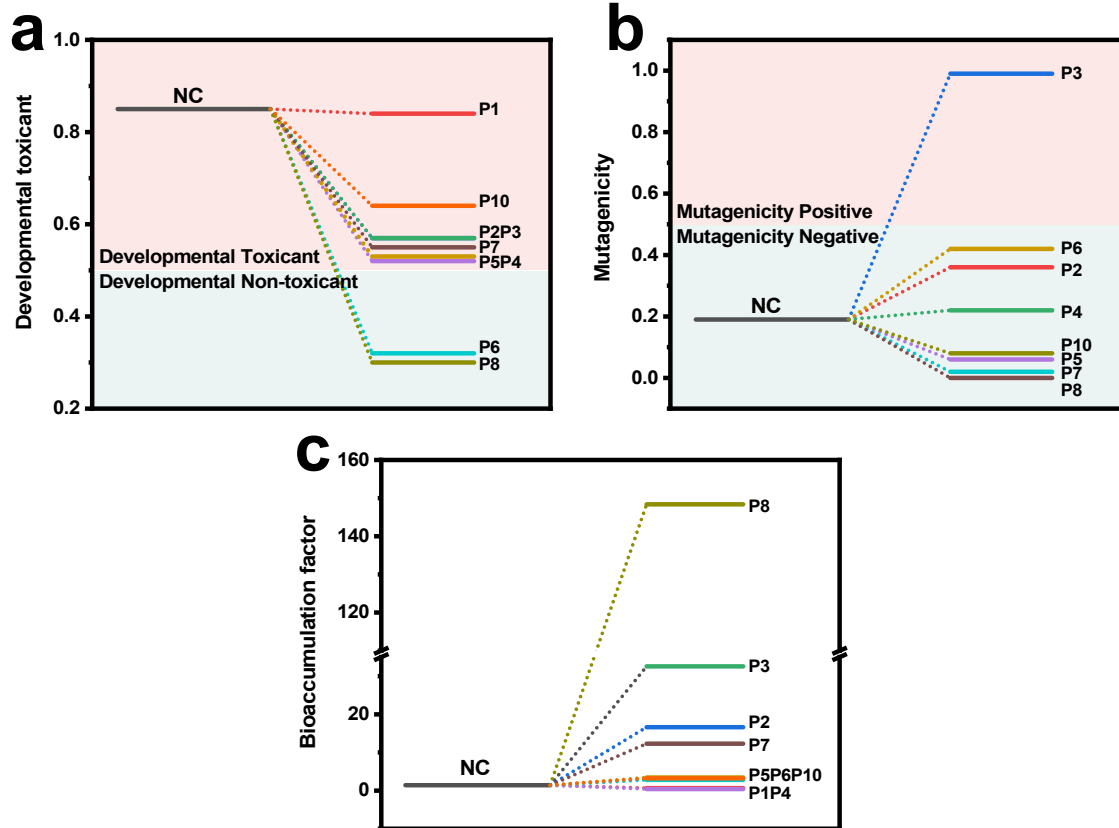


Fig. S17 (a-c) Developmental toxicity, mutagenicity and bioaccumulation factor of NC and the intermediates by T.E.S.T software in Ag-PANI@PAS/PDS system.

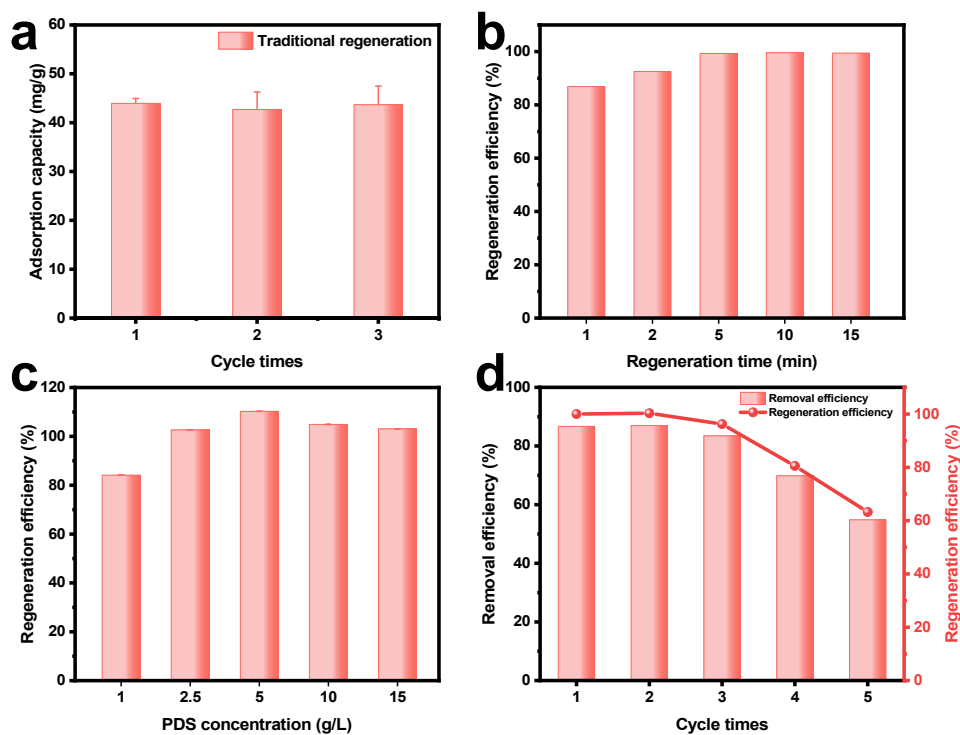


Fig. S18 (a) Recyclability of the Ag-PANI@PAS by traditional method. (b) The regeneration time on the regeneration effect (NC = 200 $\mu\text{mol}\cdot\text{L}^{-1}$, [PDS] = 5 $\text{g}\cdot\text{L}^{-1}$). (c) The PDS dosage on the regeneration effect (NC = 200 $\mu\text{mol}\cdot\text{L}^{-1}$, regeneration time = 5 min). (d) Regeneration times of Ag-PANI@PAS in the PDS system (NC = 200 $\mu\text{mol}\cdot\text{L}^{-1}$, [PDS] = 2.5 $\text{g}\cdot\text{L}^{-1}$, regeneration time = 5 min).

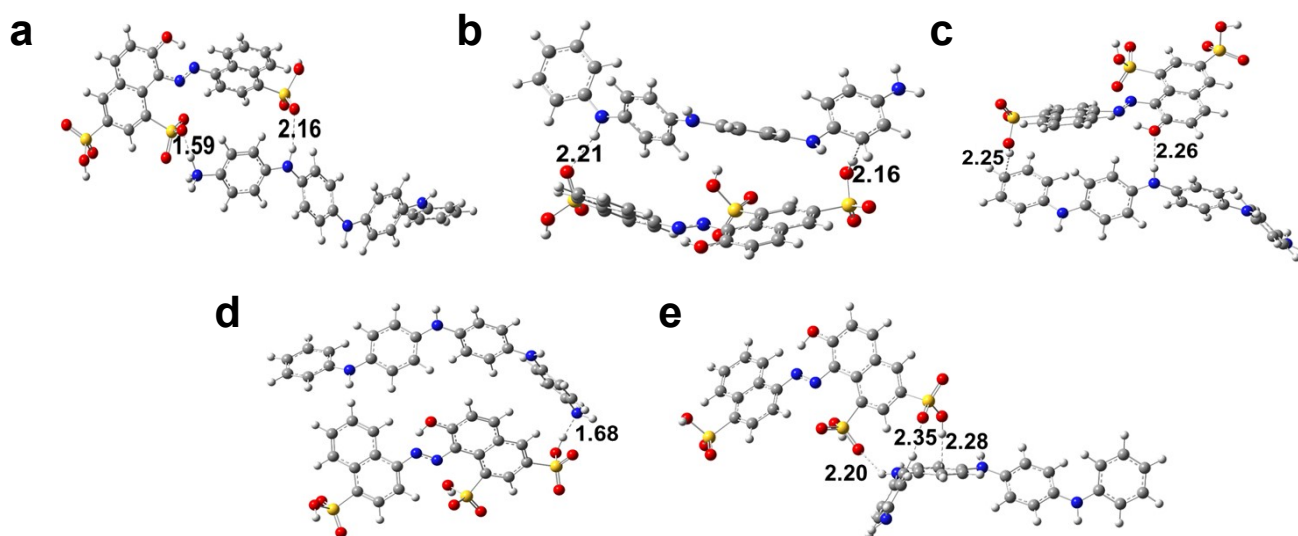


Fig. S19 Potential interactions between NC and PANI polymers.

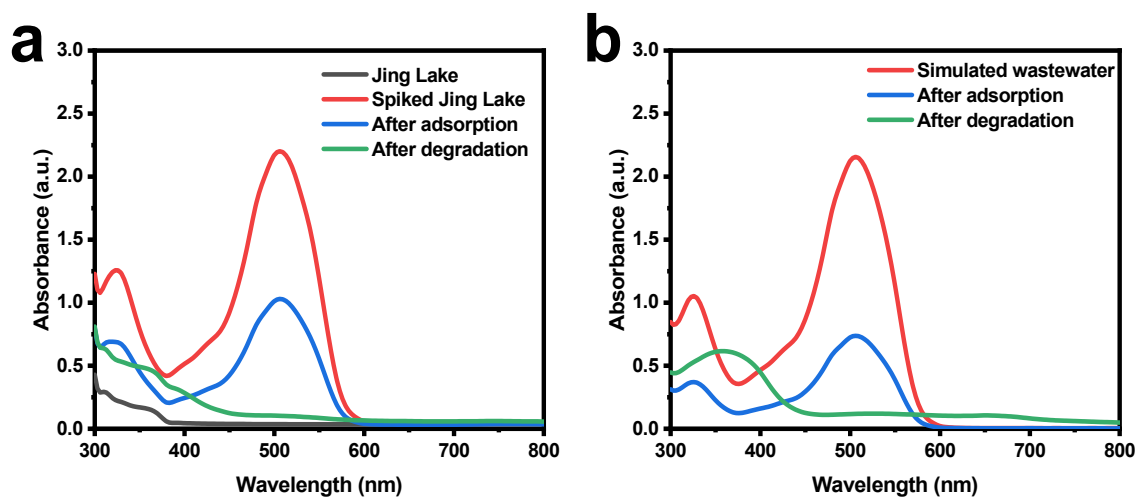


Fig. S20 UV-vis spectra of different water matrices on the removal of NC in Ag-PANI@PAS/PDS process.

Table S1 The loading of Ag-PANI on different sponges

	PUS	MS	PAS	Ag-PANI@PUS	Ag-PANI@MS	Ag-PANI@PAS
m (mg)	21.7	8.87	7.78	18.3	9.17	9.70
Δm (mg)	/	/	/	-3.38	0.30	1.92
Average load ratio (%)	/	/	/	n.c.	3.27	24.7

n.c.: no calculation.

Table S2 Isotherm parameters for adsorption

	Langmuir isotherm				Freundlich isotherm		
	Q_m ($\text{mg}\cdot\text{g}^{-1}$)	K_L ($\text{L}\cdot\text{mg}^{-1}$)	R_L	R^2	$1/n$	K_F ($\text{mg}^{1-n}\cdot\text{g}^{-1}\cdot\text{L}^n$)	R^2
Ag-PANI@PAS	47.6	0.346	0.02-0.32	0.978	0.351	15.0	0.876

Table S3 Kinetics parameters for adsorption

	Pseudo-first-order model			Pseudo-second-order model		
	$Q_{e,cal}$ (mg·g ⁻¹)	k_1 (min ⁻¹)	R^2	$Q_{e,cal}$ (mg·g ⁻¹)	k_2 (g·mg ⁻¹ ·min ⁻¹)	R^2
Ag-PANI@PAS	5.33	0.032	0.941	14.1	0.035	0.998

Table S4 Kinetic fit correlation coefficient (R^2) of Ag-PANI@PAS

	Catalytic kinetics model		Adsorption kinetics model	
	Primary kinetics	Secondary kinetics	Pseudo-first-order	Pseudo-second-order
NC	0.968	0.733	0.838	0.948

Table S5 Chemical composition of the simulated wastewater

Compound	Concentration (mg·L ⁻¹)
NC	120
NaCl	10
Na ₂ SO ₄	10
Na ₂ CO ₃	10
KCl	10
KNO ₃	10
CH ₃ COONa	10
Sodium dodecyl sulfate	10
Sodium carboxymethyl cellulose	10

References

- 1 A. H. Memon, B. Wei, S. Shams, Y. Jiang, M. Jiao, M. Su and H. Liang, *Catal. Sci. Technol.*, 2022, **12**, 2846-2855.
- 2 K. Zhu, X. Wang, D. Chen, W. Ren, H. Lin and H. Zhang, *Chemosphere*, 2019, **231**, 32-40.
- 3 L. Guo, L. Zhao, Y. Tang, J. Zhou and B. Shi, *J. Environ. Chem. Eng.*, 2022, **10**, 106979.